INTERNATIONAL JOURNAL FOR NUMERICAL METHODS IN FLUIDS
Int. J. Numer. Meth. Fluids 2009; **60**:119–148
Published online 7 August 2008 in Wiley InterScience (www.interscience.wiley.com). DOI: 10.1002/fld.1873

Study of water waves with submerged obstacles using a vortex method with Helmholtz decomposition

M. Y. Lin*, † and L. H. Huang

Department of Civil Engineering, National Taiwan University, Taipei 10617, Taiwan, Republic of China

SUMMARY

The present study develops a 2-D numerical scheme that combines the vortex method and the boundary integral method by a Helmholtz decomposition to investigate the interaction of water waves with submerged obstacles. Viscous effects and generation of vorticity on the free surface are neglected. The second kind of Fredholm integral equations that govern the strengths of vortex sheets along boundaries are solved iteratively. Vorticity is convected and diffused in the fluid via a Lagrangian vortex (blob) method with varying cores, using the particle strength exchange method for diffusion, with particle redistribution. A grid-convergence study of the numerical method is reported. The inviscid part of the method and the simulation of the free-surface motion are tested using two calculations: solitary wave propagation in a uniform channel and a moving line vortex in the fluid. Finally, the full model is verified by simulating periodic waves travelling over a submerged rectangular obstacle using nonuniform vortex blobs with a mapping of the redistribution lattice. Overall, the numerical model predicts the vortices' evolution and the free-surface motion reasonably well. Copyright © 2008 John Wiley & Sons, Ltd.

Received 16 May 2007; Revised 27 May 2008; Accepted 28 May 2008

KEY WORDS: free surface; vortex motion; fluid–structure interaction; vortex methods; boundary integral methods

1. INTRODUCTION

The interaction of surface water waves with submerged structures has attracted attention in many fields of engineering applications. Especially in coastal engineering, the protection against beach erosion by submerged breakwaters with reduced environmental and visual impacts has been an important topic in recent years. Numerous theoretical and numerical studies for this problem have

*Correspondence to: M. Y. Lin, Department of Civil Engineering, National Taiwan University, Taipei 10617, Taiwan, Republic of China.
†E-mail: mylin@mac.com

Contract/grant sponsor: National Science Council of R.O.C.; contract/grant numbers: NSC 92-2611-E-002-030, NSC 93-2611-E-002-012

been implemented based on potential-flow theory with the assumption that the flow is irrotational [1–10]. Chan *et al*. [11] implemented the analytic investigation of linear, viscous water waves with the assumption that flow is essentially irrotational except in the unseparated boundary layers adjacent to solid and free-surface boundaries. One of the benefits of the approaches using the irrotational-flow assumption is the efficient computation by applying boundary integral methods, and these approaches usually predict the transformation of water waves accurately if flow separation is not severe.

However, for the study of flow field around a bluff body, the effects of flow separation cannot be neglected. Owing to this reason, numerous numerical schemes for solving free-surface flow with viscous effects have been developed. Many researchers have studied this problem by solving the Navier–Stokes equations for laminar flows or the Reynolds averaged Navier–Stokes equations with turbulence closure for turbulent flows using various numerical schemes such as finite difference methods [12, 13], finite-analytic methods [14, 15], finite volume methods [16–18] and finite element methods [19–21]. These numerical methods are all grid-based schemes. In the schemes using a moving mesh, it is necessary to update the grid points every time step in order to cooperate with the moving free-surface boundary, and it may introduce additional numerical errors. Even if a Eulerian method with fixed grid points is applied, it may be difficult to track the fluid interface and enforce the free-surface boundary conditions. On the other hand, using a grid-based scheme, it is necessary to set a sufficient resolution near submerged bodies to capture vorticity generation and evolution; otherwise, the strength of the generated vortices may be underestimated by the insufficient resolution and the induced numerical dissipation. A Lagrangian, grid-free vortex (particle) method [22] is an alternative scheme to avoid the errors from the insufficient grid resolution and the numerically dissipative truncation for a viscous-flow simulation. However (to the best of our knowledge), very few researchers have extended vortex methods to the simulation of free-surface flow. Lundgren and Koumoutsakos [23] have investigated an application of vortex methods for viscous free-surface flows, but their aim was to study the mechanism for the generation of vorticity at the free surface and did not present any computational result.

This paper focuses on the numerical study of vortex generation and evolution induced by 2-D free-surface flow passing over submerged obstacles. Since for most problems in water-wave mechanics the free-surface viscosity is negligible, at the free surface we ignore the effect of viscosity and the generation of vorticity. In this study an essentially grid-free numerical model is developed. The motivation is based on the fact that in water-wave problems the flow field far from submerged bodies can be simplified to be irrotational and may be treated by including a viscous-flow correction to the potential-flow analysis. To accomplish this, we apply the Helmholtz decomposition [1] to decompose the flow field into two components: one related to the vorticity (vortical velocity) and the other being irrotational. It should be noted that the two components are not solved independently because they affect each other. In this study, a vortex method that determines the viscous-flow dynamics by attaching the vorticity to the computational elements (vortex particles) is applied to simulate the vortical velocity field. In contrast with grid-based schemes, the Lagrangian vortex particles convect without numerical dissipation and automatically adjust to resolve the regions with vorticity. The distribution of dipole (vortex sheet) along the free surface determines the irrotational flow field, and the vortex sheet along the solid surface determines the vorticity flux into the fluid. The strengths of these singularities are solved iteratively by a boundary integral method based on the approach proposed by Baker *et al*. [24].

In Section 2 the mathematical formulations for solving the alternative variables instead of the primitive ones are presented. In Section 3 we describe the numerical formulations and the solution

DOI: 10.1002/fld

procedure of the proposed method. In Section 4 the verifications of the method and an application to periodic water waves over a rectangular submerged obstacle are described. Finally, conclusions of the present study are given in Section 5.

2. MATHEMATICAL FORMULATIONS

2.1. Governing equations

Here, we consider 2-D flow in a uniform channel with a free surface and a submerged obstacle (see Figure 1(a). Figure 1(b)–(c) will be referred later). The fluid is assumed to be incompressible with constant density and viscosity. The motion of fluid is governed by the continuity equation and the Navier–Stokes equations in terms of the velocity $\mathbf{u}$ and the pressure p:

$$\nabla \cdot \mathbf{u} = 0 \tag{1}$$

$$\frac{\mathrm{D}\mathbf{u}}{\mathrm{D}t} = -\frac{1}{\rho}\nabla p - g\hat{\mathbf{j}} + \nu\nabla^2\mathbf{u} \tag{2}$$

with the material derivative defined as

$$\frac{\mathrm{D}}{\mathrm{D}t} = \frac{\partial}{\partial t} + \mathbf{u}\cdot\nabla \tag{3}$$

where $\hat{\mathbf{j}}$ is the unit vector that points vertically upwards, ρ the density, g the gravitational acceleration, ν the molecular viscosity and $\mathbf{x} = (x, y)$, $\mathbf{u} = (u, v)$.

By taking the curl of each term in (2) and using (1), we obtain the vorticity transport equation

$$\frac{\mathrm{D}\omega}{\mathrm{D}t} = \nu\nabla^2\omega \tag{4}$$

with the concept of vorticity $\boldsymbol{\omega} = (0, 0, \omega)$ defined as

$$\boldsymbol{\omega} = \nabla \times \mathbf{u} \tag{5}$$

2.2. Boundary conditions

2.2.1. Solid-surface boundary condition. On the impermeable, solid surface $\mathbf{x}_\mathrm{B}$, flow kinematics dictates that the normal component of the flow velocity must be equal to the normal component of the solid-surface velocity $\mathbf{U}_\mathrm{B}$:

$$\mathbf{u}(\mathbf{x}_\mathrm{B})\cdot\hat{\mathbf{n}} = \mathbf{U}_\mathrm{B}(\mathbf{x}_\mathrm{B})\cdot\hat{\mathbf{n}} \tag{6}$$

The boundary condition for the tangential component of the velocity results from the effect of molecular viscosity, enforcing that the tangential components of the velocity of the fluid and the velocity of the solid surface are the same:

$$\mathbf{u}(\mathbf{x}_\mathrm{B})\cdot\hat{\mathbf{t}} = \mathbf{U}_\mathrm{B}(\mathbf{x}_\mathrm{B})\cdot\hat{\mathbf{t}} \tag{7}$$

The two equations compose the no-slip boundary condition on a solid surface:

$$\mathbf{u}(\mathbf{x}_\mathrm{B}) = \mathbf{U}_\mathrm{B}(\mathbf{x}_\mathrm{B}) \tag{8}$$

DOI: 10.1002/fld

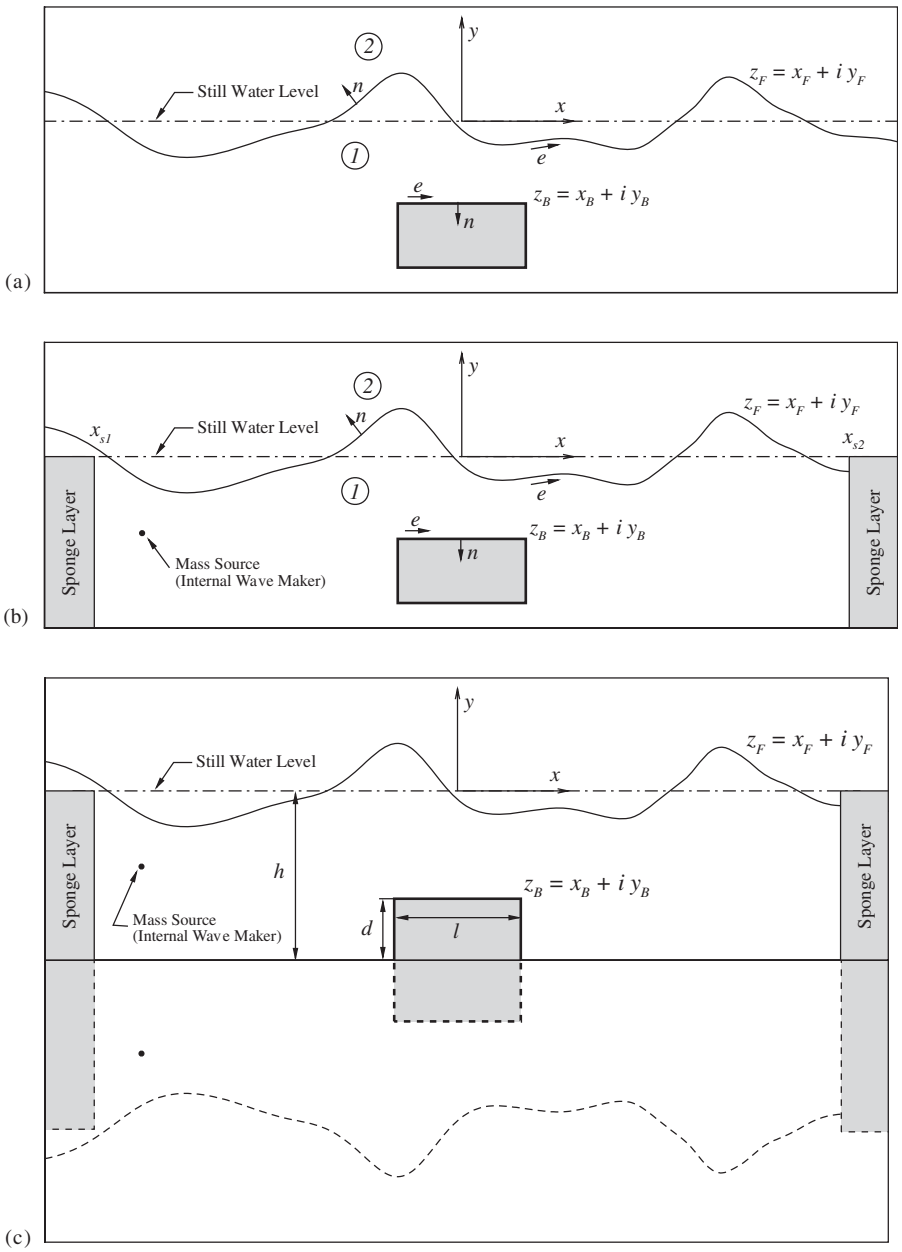

Figure 1. Definition sketch for water waves over a submerged obstacle: (a) original setup; (b) definition sketch with sponge layers and an internal wave-maker; and (c) definition sketch in which the method of image is used.

DOI: 10.1002/fld

2.2.2. Kinematic free-surface boundary condition. At the free surface there must be no flow across the interface. This leads to its kinematic free-surface boundary condition (KFSBC). In a Lagrangian aspect, it gives

$$\frac{\mathrm{D}\mathbf{x}_\mathrm{F}}{\mathrm{D}t} = \mathbf{u}(\mathbf{x}_\mathrm{F}) \tag{9}$$

where $\mathbf{x}_\mathrm{F}$ denotes the free-surface points.

2.2.3. Dynamic free-surface boundary condition. The dynamic free-surface boundary condition (DFSBC) is determined by the continuity of pressure across the free surface and the momentum equation (2) in which the free-surface viscosity is ignored:

$$\frac{\mathrm{D}\mathbf{u}}{\mathrm{D}t}(\mathbf{x}_\mathrm{F}) = -\frac{1}{\rho}\nabla p - g\nabla(\mathbf{x}_\mathrm{F}\cdot\hat{\mathbf{j}}) \quad \text{with } p = p_\mathrm{atm} \tag{10}$$

where p_atm is the atmospheric pressure.

2.2.4. Lateral boundary condition. From a mathematical aspect, the lateral boundaries are extended to infinity to avoid wave reflection, but numerically we have to truncate the computational domain into a limited region. For this reason, numerical sponge layers are used at both lateral boundaries to absorb the outward-traveling waves. Furthermore, to generate specific wave trains a designed mass source is set in the flow region near the left boundary. The details are presented in Section 3.3.

2.3. Integral formulations of Helmholtz decomposition

Applying the integral formulations of the Helmholtz decomposition (a detailed description is presented in the Appendix), fluid velocity can be expressed as

$$\begin{aligned}\mathbf{u}(\mathbf{x}) &= \int_V \omega(\mathbf{x}')\hat{\mathbf{k}}\times\nabla G\,\mathrm{d}\mathbf{x}' + \int_{S_\mathrm{F}} \Gamma_\mathrm{F}(\mathbf{x}')\hat{\mathbf{k}}\times\nabla G\,\mathrm{d}\mathbf{x}' \\ &= \int_V \omega(\mathbf{x}')\hat{\mathbf{k}}\times\nabla G\,\mathrm{d}\mathbf{x}' + \nabla\int_{S_\mathrm{F}} \mu(\mathbf{x}')\frac{\partial G}{\partial n(\mathbf{x}')}\,\mathrm{d}\mathbf{x}'\end{aligned} \tag{11}$$

where Γ_F and μ are, respectively, the strength of the vortex sheet and dipole, S_F indicates the free surface and G is the fundamental solution of Laplace's equation given by

$$G = G(\mathbf{x},\mathbf{x}') = \frac{1}{2\pi}\ln|\mathbf{x}-\mathbf{x}'| \tag{12}$$

We may note that in Equation (11) the boundary integral is only over the free surface, and the surface distribution of dipoles is equivalent to a vortex sheet. In fact, in 2-D flow the vortex-sheet strength is related to the arclength derivatives of the dipole strength [24].

From this integral formulation, we may construct an alternative well-posed problem for $\mathbf{x}_\mathrm{F}$, Γ_F and ω expressed by the following set of governing equations and boundary conditions:

$$\frac{\mathrm{D}\mathbf{x}_\mathrm{F}}{\mathrm{D}t} = \mathbf{u}(\mathbf{x}_\mathrm{F}) \quad \text{on } S_\mathrm{F} \tag{13a}$$

$$\frac{\partial\Gamma_\mathrm{F}}{\partial t} = \mathbb{F}(\Gamma_\mathrm{F},\omega,\mathbf{x}_\mathrm{F},t) \quad \text{on } S_\mathrm{F} \tag{13b}$$

DOI: 10.1002/fld

$$\frac{\mathrm{D}\omega}{\mathrm{D}t} = \nu\nabla^2\omega \quad \text{in } V \tag{13c}$$

$$\mathbf{u}(\mathbf{x}_\mathrm{B}) = \mathbf{U}_\mathrm{B}(\mathbf{x}_\mathrm{B}) \quad \text{on } S_\mathrm{B} \tag{13d}$$

Equation (13a) is the KFSBC, which is used to solve the free-surface position $\mathbf{x}_\mathrm{F}$. Equation (13b), an evolution equation for solving Γ_F, will be derived in Section 2.5 from the DFSBC. The vorticity field ω is governed by the vorticity transport equation (13c), enforcing the no-slip boundary condition (13d) on the solid surface.

2.4. Viscous splitting algorithm for the vorticity boundary condition

Since a vortex method is used to solve the vorticity field, in the present study a treatment for the no-slip boundary condition in the context of vortex methods is required. Following the so-called 'viscous splitting algorithm' in vortex methods [22, Chapter 6], equation set (13) is solved by a fractional step. Consider that in the time interval $[t_n, t_{n+1}]$ the flow is advanced from t_n to t_{n+1}, and vorticity fields ω_1 and ω_2 are the solutions of vorticity solved by the following two substeps:

Substep 1—free surface and existent vorticity transportation:

$$\frac{\mathrm{D}\mathbf{x}_\mathrm{F}}{\mathrm{D}t} = \mathbf{u}(\mathbf{x}_\mathrm{F}) \quad \text{on } S_\mathrm{F} \tag{14a}$$

$$\frac{\partial\Gamma_\mathrm{F}}{\partial t} = \mathbb{F}(\Gamma_\mathrm{F}, \Gamma_\mathrm{B}, \omega_1, \mathbf{x}_\mathrm{F}, t) \quad \text{on } S_\mathrm{F} \tag{14b}$$

$$\mathbf{u}\cdot\hat{\mathbf{n}} = \mathbf{U}_\mathrm{B}\cdot\hat{\mathbf{n}} \;\Rightarrow\; \frac{\partial\Gamma_\mathrm{B}}{\partial t} = \mathbb{H}(\Gamma_\mathrm{F}, \Gamma_\mathrm{B}, \omega_1, \mathbf{x}_\mathrm{F}, t) \quad \text{on } S_\mathrm{B} \tag{14c}$$

$$\frac{\mathrm{D}\omega_1}{\mathrm{D}t} = \nu\nabla^2\omega_1 \quad \text{in } V \tag{15a}$$

$$\omega_1(\cdot, t_n) = \omega_n \quad \text{in } V \tag{15b}$$

$$\frac{\partial\omega_1}{\partial n} = 0 \quad \text{on } S_\mathrm{B} \tag{15c}$$

In this substep, since only the normal component of the solid-surface boundary condition is applied, on S_B there is no net vorticity produced into the fluid and a 'spurious' vortex sheet Γ_B induced by the slip velocity on S_B appears in order to enforce the no-penetration boundary condition. The evolution equation for Γ_B, Equation (14c), will be derived in Section 2.5.

Substep 2—vorticity creation:

$$\frac{\mathrm{D}\omega_2}{\mathrm{D}t} = \nu\nabla^2\omega_2 \quad \text{in } V \tag{16a}$$

$$\omega_2(\cdot, t_n) = 0 \quad \text{in } V \tag{16b}$$

$$\nu\frac{\partial\omega_2}{\partial n} = \hat{\mathbf{t}}\cdot\frac{\mathrm{D}(\mathbf{u}_\mathrm{slip} - \mathbf{U}_\mathrm{B})}{\mathrm{D}t} \quad \text{on } S_\mathrm{B} \tag{16c}$$

DOI: 10.1002/fld

Here, $\mathbf{u}_{\text{slip}}$ is the slip velocity on the solid surface, solved in Substep 1. Equation (16c) indicates the vorticity flux on S_B to cancel the slip velocity. This is the completion of one time step of the proposed algorithm, with the vorticity field $\omega_{n+1}=\omega_1(\cdot,t_{n+1})+\omega_2(\cdot,t_{n+1})$ and the velocity field evaluated by Equation (11).

2.5. *Evolution equations for* Γ_F *and* Γ_B

The evolution equations for Γ_F and Γ_B are derived following the approach proposed by Baker *et al*. [24] and are modified to be able to involve the effect of vorticity in the fluid. Since the vorticity field is discretized by a set of vorticity-carrying particles, from Equation (11) we find that fluid velocity can be expressed by a scalar velocity potential composed of a set of point vortices in the fluid and a dipole (vortex) distribution along S_F. In addition, due to the implementation of the viscous splitting algorithm, along S_B a spurious vortex distribution should be included. The scalar velocity potential is

$$\phi(x,y)=\int_{S_F}\mu(e)\frac{\partial G}{\partial n}s_{Fe}\,de+\frac{1}{2\pi}\int_{S_B}\Gamma_B(e)\tan^{-1}\frac{y-y(e)}{x-x(e)}s_{Be}\,de$$
$$+\frac{1}{2\pi}\sum_{j=1}^{N}\Gamma_j\tan^{-1}\frac{y-y_j}{x-x_j}+\frac{m_I(t)}{2\pi}\ln[(x-x_I)^2+(y-y_I)^2]^{1/2} \tag{17}$$

where $s_F=|\mathbf{x}_F\cdot\mathbf{x}_F|$, $s_B=|\mathbf{x}_B\cdot\mathbf{x}_B|$ and the subscript e denotes differentiation with respect to the label e, which is chosen to be a Lagrangian variable along the free surface. The contribution from the vorticity field is represented by the potential induced by N point vortices, which are characterized by their positions $\mathbf{x}_j$ and circulations Γ_j. The last term on the right-hand side of Equation (17) is an added point source located at $\mathbf{x}_I$ with the time-varying strength $m_I(t)$, prescribed to generate wave trains if an internal wave-maker is used.

For convenience, herein we introduce the complex notation $z=x+\mathrm{i}y$ for the complex field point and $q=u+\mathrm{i}v$ for the complex velocity. We also define the unnormalized vortex-sheet strength $\gamma_B=\Gamma_B s_{Be}$ to simplify the following formulations. Therefore, the Lagrangian motion of the free surface, which satisfies the KFSBC (14a) is given by

$$\frac{\partial z_F}{\partial t}(e)\equiv\tilde{q}(e)=q(e)+\frac{\alpha\gamma_F(e)}{2\bar{z}_{Fe}(e)} \tag{18}$$

where $\tilde{q}$ is the weighted average of the velocities across the free surface, determined by the last term on the right-hand side of Equation (18) with $|\alpha|\leqslant 1$ being the weighting factor and $\bar{z}$ indicating the complex conjugate of z. The average complex velocity at the free surface, $q(e)$, is given by

$$\bar{q}(e)=\frac{1}{2\pi\mathrm{i}}\mathrm{PV}\int_{S_F}\gamma_F(e')K(z_F(e),z_F(e'))\,de'+\frac{1}{2\pi\mathrm{i}}\int_{S_B}\gamma_B(e')K(z_F(e),z_B(e'))\,de'$$
$$+\frac{1}{2\pi\mathrm{i}}\sum_{j=1}^{N}\Gamma_j K(z(e),z_j)+\frac{\partial S_I}{\partial z}(z_F(e)) \tag{19}$$

DOI: 10.1002/fld

Here, PV indicates the principal value of the singular integral, $K(z,z')\equiv 1/(z-z')$, $\gamma_{\mathrm{F}}(e)=\Gamma_{\mathrm{F}}(e)s_{\mathrm{F}e}=\mu_e$, and

$$S_I(z,t)=\frac{m_I(t)}{2\pi}\ln(z-z_I) \tag{20}$$

The Lagrangian motion of $z_{\mathrm{F}}(e)$ follows the lower or upper fluid when $\alpha=1$ or -1, respectively, and $-1<\alpha<1$ chooses some weighted average of the two. The choice of the weighting factor that determines the tangential velocity for the Lagrangian markers is at our disposal (see [25] for detailed discussion). Instead of Equation (14a), Equation (18) is used as the kinematic evolution equation for the free-surface markers.

The DFSBC (10) can be expressed as the Bernoulli equation that governs the change in the potential on either side of the free surface and leads to the evolution equation for γ_{F} as

$$\frac{\partial\gamma_{\mathrm{F}}}{\partial t}=\frac{\alpha}{2}\frac{\partial}{\partial e}\frac{\gamma_{\mathrm{F}}^2}{z_{\mathrm{F}e}\bar{z}_{\mathrm{F}e}}-2A\left[\Re\left\{\frac{\partial\bar{q}}{\partial t}z_{\mathrm{F}e}\right\}-\frac{\alpha}{2}\gamma_{\mathrm{F}}\Re\left\{\frac{q_e}{z_{\mathrm{F}e}}\right\}+\frac{1}{8}\frac{\partial}{\partial e}\frac{\gamma_{\mathrm{F}}^2}{z_e\bar{z}_e}+g\,y_{\mathrm{F}e}\right] \tag{21}$$

where A is the Atwood ratio defined as the difference in the density of water and air divided by their sum. For water-wave problems we may set $A=1$. On the right-hand side of Equation (21), the first four terms arise from the dynamic-pressure term of the Bernoulli equation, and the last term is from the hydrostatic pressure. Equation (21) is substituted for Equation (14b) as the evolution equation for Γ_{F}.

On the solid surface, the normal velocity component should be continuous across the interface so that the no-through-flow boundary condition (14c) can be imposed. This condition can also be expressed alternatively in terms of the tangential velocity component, leading to a Fredholm integral equation of the second kind [22]. The condition that has to be imposed to satisfy the no-through-flow boundary condition on S_{B} is

$$\Re\{z_{\mathrm{B}e}\bar{q}_{\mathrm{B}}\}=0 \tag{22}$$

where q_{B} is the fluid velocity at the solid boundary. By differentiating Equation (22) in time, we obtain the evolution equation for γ_{B} as

$$\begin{aligned}\frac{\partial\gamma_{\mathrm{B}}}{\partial t}(e)=2\Re\Bigg\{&\frac{z_{\mathrm{B}e}(e)}{2\pi\mathrm{i}}\int_{S_{\mathrm{F}}}\frac{\partial\gamma_{\mathrm{F}}}{\partial t}(e')K(z_{\mathrm{B}}(e),z_{\mathrm{F}}(e'))\,\mathrm{d}e'\\&+\frac{z_{\mathrm{B}e}(e)}{2\pi\mathrm{i}}\mathrm{PV}\int_{S_{\mathrm{B}}}\frac{\partial\gamma_{\mathrm{B}}}{\partial t}(e')K(z_{\mathrm{B}}(e),z_{\mathrm{B}}(e'))\,\mathrm{d}e'\\&+\frac{z_{\mathrm{B}e}(e)}{2\pi\mathrm{i}}\int_{S_{\mathrm{F}}}\gamma(e')\frac{\partial K}{\partial t}(z_{\mathrm{B}}(e),z_{\mathrm{F}}(e'))\,\mathrm{d}e'+\frac{z_{\mathrm{B}e}(e)}{2\pi\mathrm{i}}\sum_{j=1}^{N}\frac{\mathrm{d}\Gamma_j}{\mathrm{d}t}K(z_{\mathrm{B}}(e),z_j)\\&+\frac{z_{\mathrm{B}e}(e)}{2\pi\mathrm{i}}\sum_{j=1}^{N}\Gamma_j\frac{\partial K}{\partial t}(z_{\mathrm{B}}(e),z_j)+z_{\mathrm{B}e}(e)\frac{\partial^2 S_I}{\partial t\,\partial z}(z_{\mathrm{B}}(e))\Bigg\}\end{aligned} \tag{23}$$

Again, Equation (23) is substituted for Equation (14c) as the evolution equation for Γ_{B}.

Equations (21) and (23) are coupled Fredholm integral equations of the second kind and can be solved efficiently in both storage and work by iteration (see [24] for detailed proof).

DOI: 10.1002/fld

3. NUMERICAL IMPLEMENTATION

First of all, in Section 3.1 we introduce the vortex method that is used in the present model to solve equation sets (15) and (16). In Section 3.2 the iteration scheme for solving γ_F and γ_B and the solution procedure of the integrated model are presented. Other numerical techniques and treatments applied in this model are shown in Sections 3.3–3.6.

3.1. The vortex method for 2-D flows

The vorticity transportation and creation are solved via the vortex method proposed by Ploumhans and Winckelmans [26]. In this method, vortex blobs may be with spatially varying cores, and the particle strength exchange (PSE) for diffusion is done in the physical domain. Based on this method, the vorticity field governed by systems (15) and (16) is solved in a Lagrangian frame to convect the vorticity-carrying fluid elements ($\mathbf{x}_i$) and then to update their strength

$$\frac{\mathrm{d}\mathbf{x}_i}{\mathrm{d}t} = \mathbf{u}(\mathbf{x}_i, t) \tag{24}$$

$$\frac{\mathrm{d}\omega}{\mathrm{d}t} = \nu\nabla^2\omega \tag{25}$$

The vorticity field is discretized to obtain a numerical approximation by N particles:

$$\omega(\mathbf{x}, t) = \sum_{j=1}^{N} \eta_j(\mathbf{x}-\mathbf{x}_j)\Gamma_j \tag{26}$$

and each particle is characterized by its position $\mathbf{x}_j(t)$ and circulation $\Gamma_j(t)$. η_j is a distribution function. In this study a Gaussian distribution is used:

$$\eta_j(\mathbf{x}) = \frac{1}{2\pi\varepsilon_j^2}\exp\left(-\frac{|\mathbf{x}|^2}{2\varepsilon_j^2}\right) \tag{27}$$

where the quantity ε_j is a measure of the core radius of the vortex.

Subsequently, the right-hand sides of Equations (24) and (25) are replaced by integral operators and then discretized by vortex particles. By applying Equations (11) and (26), Equation (24) can be expressed as

$$\frac{\mathrm{d}\mathbf{x}_i}{\mathrm{d}t} = -\sum_{j=1}^{N} \frac{\varrho(|\mathbf{x}_i-\mathbf{x}_j|/\varepsilon_{ij})}{|\mathbf{x}_i-\mathbf{x}_j|^2}(\mathbf{x}_i-\mathbf{x}_j)\times\hat{\mathbf{k}}\,\Gamma_j + \int_{S_F}\gamma_F(e')\hat{\mathbf{k}}\times\nabla G(\mathbf{x}_i, \mathbf{x}_F(e'))\,\mathrm{d}e' \tag{28}$$

where $\varrho(y) = 1/2\pi(1-\exp(-y^2/2))$ and $\varepsilon_{ij}^2 = (\varepsilon_i^2+\varepsilon_j^2)/2$. A direct computation for the first term on the right-hand side of Equation (28) requires $\mathcal{O}(N^2)$ work and is prohibitively expensive. In this study, a code using the fast multipole method [27] that has a 'theoretical' operation count of $\mathcal{O}(N)$ is developed to reduce the computation cost. In the fast algorithm the maximum number of terms P needed in the expansion to a given accuracy ε is chosen such that [27–29]

$$\left(\sum_i |\Gamma_i|\right)2^{-P} \leqslant \varepsilon$$

DOI: 10.1002/fld

In this study $P=10$ is used. Although the optimal $\mathcal{O}(N)$ behavior is not exhibited in the present study because a big overhead is required due to the multipole and Taylors expansions, significant saving of CPU time is indeed achieved.

The diffusion of the existent vorticity in the fluid is implemented by the technique of PSE:

$$\left.\frac{\mathrm{d}\Gamma_i}{\mathrm{d}t}\right|_{\mathrm{PSE}} = 2\nu \sum_{j=1}^{N} \frac{1}{\varepsilon_{ij}^2} (S_i\Gamma_j - S_j\Gamma_i)\eta_{ij}(\mathbf{x}_i - \mathbf{x}_j) \tag{29}$$

where S_i is the area of fluid associated with the particle i, and

$$\eta_{ij}(\mathbf{x}) = \frac{1}{2\pi\varepsilon_{ij}^2} \exp\left(-\frac{|\mathbf{x}|^2}{2\varepsilon_{ij}^2}\right) \tag{30}$$

In practice, the first summation in Equation (29) may not involve all N particles since η_{ij} decreases rapidly. We ignore the contribution of particles more than 5ε from $\mathbf{x}_i$.

The vorticity creation on a solid wall, i.e. the solution of equation set (16), can also be determined by an integral operator. At every time step, vorticity flux should be distributed to neighboring particles. The approximate solution proposed in [26] to determine the increasing rate of circulation from the vorticity flux at a wall and received by the particle i, $(\mathrm{d}\Gamma_i/\mathrm{d}t)|_{\mathrm{wall}}$, is used in this model.

To preserve the accuracy in the PSE scheme, one needs to maintain the condition that the particle cores overlap ($h_p/\varepsilon \leqslant 1$, with h_p the typical distance between particles) at all times. It is necessary to interpolate the vorticity field with distorted locations onto equi-spaced ($h_p \times h_p$ lattice) particle locations. If the core radius is spatially varying, the remeshing is performed in a mapped domain (see Section 4.3.2) in which the vorticity is interpolated onto a 1×1 mapped lattice. To achieve this, a remeshing scheme with the M_4' interpolation kernel introduced for the smooth particle hydrodynamics method [30] is used. In the vicinity of boundaries the decentered Λ_p' schemes [26] are used instead. In this study we use a Λ_3' kernel for particles with distance between $\frac{1}{2}h_p$ and $\frac{3}{2}h_p$, and a Λ_2' kernel for particles less than $\frac{1}{2}h_p$ from the boundary. Usually, an optimal frequency of particle redistribution needs to be obtained from numerical experiments. Moreover, redistribution is crucial to maintain the overlapping condition if blobs of variable size are used. In this study, we find that the frequency of remeshing should not be less then 2 time steps; otherwise, inappropriate oscillations of vorticity and velocity will be present.

3.2. Solution procedure

Considering the stability of the computation for the free-surface motion, we use a fourth-order Adams–Bashforth–Moulton (A.B.M.) predictor–corrector scheme to perform the time integrations for $\partial\gamma_{\mathrm{F}}/\partial t$ and $\partial z_{\mathrm{F}}/\partial t$. In addition, the first few time steps are treated with an explicit fourth-order Runge–Kutta technique. The A.B.M. scheme applied to an equation of the form $\mathrm{d}y/\mathrm{d}t = f(t)$ is

$$\begin{aligned} y_{1p} &= y_0 + \frac{\Delta t}{24}(55f_0 - 59f_{-1} + 37f_{-2} - 9f_{-3}) \\ y_{1c} &= y_0 + \frac{\Delta t}{24}(9f_{1p} + 19f_0 - 5f_{-1} + f_{-2}) \end{aligned} \tag{31}$$

DOI: 10.1002/fld

Here, f_n denotes $f(t+n\Delta t)$ and y_{1p}, y_{1c} denote the 'predicted' and 'corrected' values of y_1. The progress of vortex particles is performed explicitly using the second-order Adams–Bashforth scheme, and the vorticity creation should be implemented twice in one time interval because at the 'corrected' step an adjustment in $\partial\omega/\partial n$ is required to enforce the no-slip boundary condition.

Assume that at the nth time step (time t) all variables are known; thus, we seek to obtain their solutions at the next time step (time $t+\Delta t$). The following four-step procedure is carried out (the corresponding flow diagram is shown in Figure 2):

Step 1—(predicted) evolution of z_F, γ_F and γ_B: The evolution equations for γ_F and γ_B, Equations (21) and (23), can be expressed as

$$\frac{\partial\gamma_F}{\partial t}=\mathscr{L}_F\left(\frac{\partial\gamma_F}{\partial t},\frac{\partial\gamma_B}{\partial t}\right)+\mathscr{F}_F \tag{32}$$

$$\frac{\partial\gamma_B}{\partial t}=\mathscr{L}_B\left(\frac{\partial\gamma_F}{\partial t},\frac{\partial\gamma_B}{\partial t}\right)+\mathscr{F}_B \tag{33}$$

where $\mathscr{L}_F$, $\mathscr{L}_B$ indicate the integrals involving $\partial\gamma_F/\partial t$ and $\partial\gamma_B/\partial t$, respectively, and the remainder of the terms in (21) and (23) are represented by $\mathscr{F}_F$, $\mathscr{F}_B$, respectively. In Equations (32) and (33), spatial integrals are computed by the sums based on trapezoidal quadrature, spatial derivatives with respect to e are evaluated using cubic spline approximations and $\mathrm{d}\Gamma_j/\mathrm{d}t$ is evaluated by Equation (29). The iterative procedure to solve the nth approximation of $\partial\gamma_F/\partial t$ and $\partial\gamma_B/\partial t$ is implemented by the following equations [5]:

$$\begin{aligned}\frac{\partial\gamma_F^{(n)}}{\partial t}=&\frac{1}{2}\mathscr{L}_F\left(\frac{\partial\gamma_F^{(n-1)}}{\partial t}+\mathscr{L}_F\left(\frac{\partial\gamma_F^{(n-1)}}{\partial t},\frac{\partial\gamma_B^{(n-1)}}{\partial t}\right),\mathscr{L}_B\left(\frac{\partial\gamma_F^{(n-1)}}{\partial t},\frac{\partial\gamma_B^{(n-1)}}{\partial t}\right)\right)\\&+\mathscr{F}_F+\frac{1}{2}\mathscr{L}_F(\mathscr{F}_F,\mathscr{F}_B)\end{aligned} \tag{34}$$

$$\begin{aligned}\frac{\partial\gamma_B^{(n)}}{\partial t}=&\frac{1}{2}\mathscr{L}_B\left(\mathscr{L}_F\left(\frac{\partial\gamma_F^{(n-1)}}{\partial t},\frac{\partial\gamma_B^{(n-1)}}{\partial t}\right),\frac{\partial\gamma_B^{(n-1)}}{\partial t}+\mathscr{L}_B\left(\frac{\partial\gamma_F^{(n-1)}}{\partial t},\frac{\partial\gamma_B^{(n-1)}}{\partial t}\right)\right)\\&+\mathscr{F}_B+\frac{1}{2}\mathscr{L}_B(\mathscr{F}_F,\mathscr{F}_B)\end{aligned} \tag{35}$$

The iterative procedure is stopped when the absolute value of the difference in two successive iterates is less than 10^{-5}.

Subsequently, the predicted values of $\gamma_F(t+\Delta t)$ and $z_F(t+\Delta t)$ are obtained by the fourth-order Adams–Bashforth scheme, and the predicted $\gamma_B(t+\Delta t)$ is evaluated simply by

$$\gamma_B(t+\Delta t)=\frac{\partial\gamma_B}{\partial t}\Delta t \tag{36}$$

because in the past γ_B has been diffused into the fluid and merged into the existent vortex particles.

DOI: 10.1002/fld

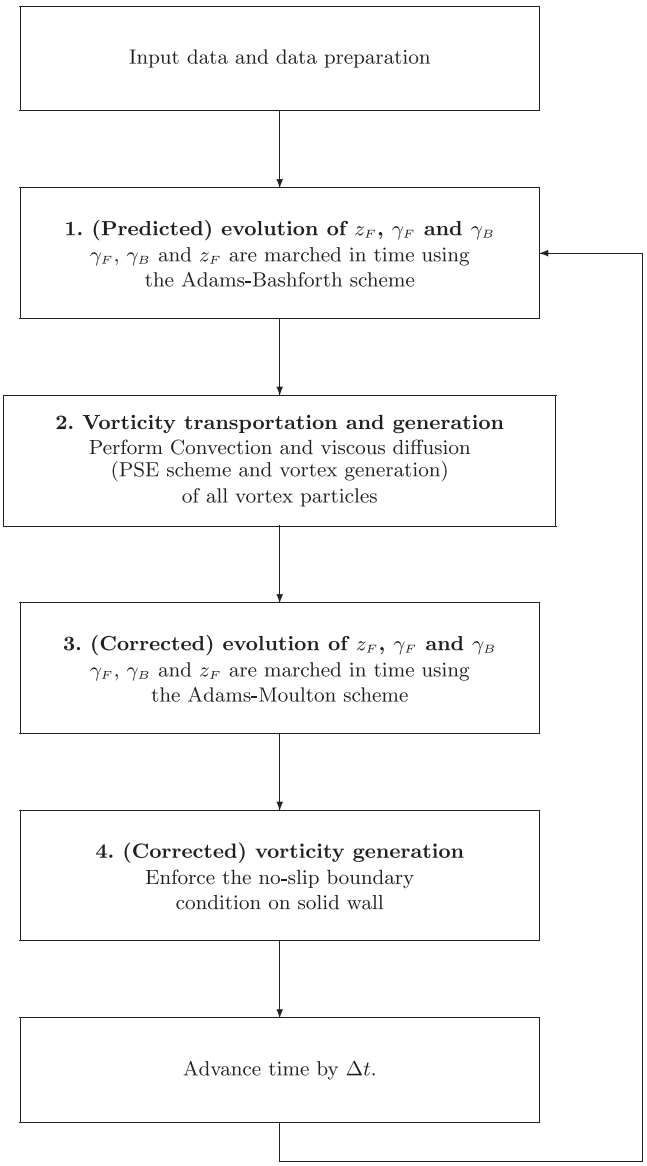

Figure 2. Flow diagram for numerical procedure.

Step 2—vorticity transportation and generation: The velocity of the vorticity-carrying particles is computed by Equation (28) and then integrated with a second-order Adams–Bashforth scheme to advance the particle positions. The strength of particles is updated by the PSE scheme and the vorticity flux from the solid wall. These can be expressed as

$$\mathbf{x}_i^{n+1} = \mathbf{x}_i^n + \Delta t\left(\tfrac{3}{2}\mathbf{u}_i(\mathbf{x}^n, \Gamma^n) - \tfrac{1}{2}\mathbf{u}_i(\mathbf{x}^{n-1}, \Gamma^{n-1})\right) \tag{37}$$

DOI: 10.1002/fld

$$\Gamma_i^* = \Gamma_i^n + \Delta t \left.\frac{\mathrm{d}\Gamma_i}{\mathrm{d}t}\right|_{\mathrm{PSE}} (\mathbf{x}^n, \Gamma^n) \tag{38}$$

$$\Gamma_i^{n+1} = \Gamma_i^* + \Delta t \left.\frac{\mathrm{d}\Gamma_i}{\mathrm{d}t}\right|_{\mathrm{wall}} (\mathbf{x}^{n+1}, \Gamma^*) \tag{39}$$

The remeshing scheme is applied every few time steps after the convection and diffusion of vortices. After each redistribution, at the new time step an Adams–Bashforth scheme is infeasible, and a second-order Runge–Kutta scheme is applied for vortex convection:

$$\mathbf{x}_i^{n+1/2} = \mathbf{x}_i^n + \Delta t\, \mathbf{u}_i(\mathbf{x}^n, \Gamma^n) \tag{40}$$

$$\Gamma_i^* = \Gamma_i^n + \Delta t \left.\frac{\mathrm{d}\Gamma_i}{\mathrm{d}t}\right|_{\mathrm{PSE}} (\mathbf{x}^n, \Gamma^n) \tag{41}$$

$$\mathbf{x}_i^{n+1} = \mathbf{x}_i^n + \tfrac{1}{2}\Delta t\,(\mathbf{u}_i(\mathbf{x}^n, \Gamma^n) + \mathbf{u}_i(\mathbf{x}^{n+1/2}, \Gamma^*)) \tag{42}$$

The update of particle strength is also performed using Equations (38) and (39).

Step 3—(corrected) evolution of z_{F}, γ_{F} *and* γ_{B}: Solve $\partial\gamma_{\mathrm{F}}/\partial t$ and $\partial\gamma_{\mathrm{B}}/\partial t$ at time $t+\Delta t$ (the corrector step) by iteration. Subsequently, the corrected values of $\gamma_{\mathrm{F}}(t+\Delta t)$ and $z_{\mathrm{F}}(t+\Delta t)$ are obtained by the fourth-order Adams–Moulton scheme, and the corrected value of $\gamma_{\mathrm{B}}(t+\Delta t)$ is evaluated by Equation (36).

Step 4—(corrected) vorticity generation: The diffusion of the (corrected) vortex sheet $\gamma_{\mathrm{B}}(t+\Delta t)$ is implemented by Equation (39) to ensure that at time $t+\Delta t$ the flow field satisfies the no-slip boundary condition on the solid surface.

After sufficiently long-term computation, instability on the computed free surface usually grows. A linear filtering scheme [31] that involves filtering z_{F} and γ_{F} is applied to remove the instability.

3.3. Wave generation and absorption

To generate periodic wave trains, we prescribe a point mass source with time-varying strength inside the numerical domain near the left boundary (Figure 1(b)). This is usually called the 'internal wave-maker' [32]. In this research, the desired wave train to generate is the second-order Stokes wave [33]:

$$y_{\mathrm{F}}(t) = \frac{H}{2}\cos\left(\frac{\pi}{2} - \omega t - p_s\right) + \frac{H^2 k}{16\sinh^3 kh}\cosh kh(2+\cosh 2kh)\cos\left[2\left(\frac{\pi}{2} - \omega t - p_s\right)\right]$$

where $k = 2\pi/L$ is the wave number; L, the wave length; $\omega = 2\pi/T$, the angular frequency; T, the wave period; H, the wave height; h, still water depth; and p_s, the phase shift constant to enforce $y_{\mathrm{F}} = 0$ at $t = 0$. Following the method proposed in [32], we may get the corresponding source function as

$$m_I(t) = \frac{LH}{T}\cos\left(\frac{\pi}{2} - \omega t - p_s\right) + \frac{LH^2 k}{8T}\frac{\cosh kh}{\sinh^3 kh}(2+\cosh 2kh)\cos\left[2\left(\frac{\pi}{2} - \omega t - p_s\right)\right] \tag{43}$$

DOI: 10.1002/fld

It should be noted that in the present study the internal wave-maker is a point source, instead of a rectangular source region with constant strength used in [32].

The sponge layer technique [5], which can reduce γ_F efficiently to zero and avoid significant wave reflections, is used to absorb outgoing waves at the truncation boundaries. We locate the sponge layers with length L_s at the left and right boundaries, $x_{s1}-L_s \leqslant x \leqslant x_{s1}$ and $x_{s2} \leqslant x \leqslant x_{s2}+L_s$ (see Figure 1(b)), and then add damping terms into Equations (18) and (21):

$$\frac{\partial z_F}{\partial t} = \tilde{q} - \mathrm{i} v_s(x) y_F \tag{44}$$

$$\frac{\partial \gamma_F}{\partial t} = R_{\gamma_F}(\gamma_F, z_F) - v_s(x)\gamma_F \tag{45}$$

where $R_{\gamma_F}(\gamma_F, z_F)$ indicates the right-hand side of Equation (21), and

$$v_s(x) = \begin{cases} v_d(x-x_{s1})^2/L_s^2, & x \leqslant x_{s1} \\ v_d(x-x_{s2})^2/L_s^2, & x \geqslant x_{s2} \\ 0 & \text{otherwise} \end{cases} \tag{46}$$

where v_d is a positive constant. The optimal values of v_d and L_s can be determined by a series of numerical tests.

3.4. Sub-grid modelling

For high-Reynolds-number flow the turbulent effect should be taken into account; otherwise, the dissipation of vorticity could be underestimated. In this paper, the turbulent eddy viscosity evaluated by a subgrid-scale model [34] is applied to simulate the effect of the subgrid-scale eddies on the larger scales. Eddy viscosity v_{eddy} is given by

$$v_{\text{eddy}} = Cs^2 \Delta^2 \sqrt{S_{ij} S_{ij}} \tag{47}$$

where S_{ij} denotes the strain rate tensor:

$$S_{ij} = \frac{1}{2}\left(\frac{\partial u_i}{\partial x_j} + \frac{\partial u_j}{\partial x_i}\right)$$

Δ is the filter length scale related to the core size of vortex particles [35] and Cs is a constant in the range of $0.1 \leqslant Cs \leqslant 0.24$. Typically $Cs = 0.15$.

3.5. Method of image for the boundary condition on the flat bottom

In this study, the bottom of the numerical wave tank is set to be flat, and a 'method of image' may be applied in Substep 1 to enforce the no-penetration boundary condition on the bottom. The schematic diagram of the image system is shown in Figure 1(c). Applying this method the fundamental solution in the integral formulation of velocity field (11) (and the related kernels in the integral equations mentioned earlier) becomes

$$\hat{G}(\mathbf{x}, \mathbf{x}') = \frac{1}{2\pi}(\ln|\mathbf{x}-\mathbf{x}'| - \ln|\mathbf{x}-\hat{\mathbf{x}}'|) \tag{48}$$

DOI: 10.1002/fld

where $\hat{\mathbf{x}}=(x,-2h-y)$. One may note that the new kernel is not applied in the PSE calculation because its integration is over the real fluid domain only.

3.6. Nondimensionalization and stability criterion

By expressing all equations in terms of nondimensional variables, one solution may suffice for a variety of different problems. After choosing the typical length D and the typical speed U and then using the following dimensionless variables

$$\mathbf{x}^*=\frac{\mathbf{x}}{D},\quad \mathbf{u}^*=\frac{\mathbf{u}}{U},\quad t^*=\frac{Ut}{D},\quad p^*=\frac{p}{\rho U^2} \tag{49}$$

the governing equations and boundary conditions can be converted into dimensionless forms. In the computation of periodic waves past a rectangular obstacle (Section 4.3), we choose the still water depth as the typical length D and evaluate the typical speed U from the incoming wave condition.

Ploumhans [36] found an upper limit on the time step for the stability of the PSE. For the Gaussian blobs with an overlap ratio $\varepsilon/h_p=1$ the limit in dimensionless form is

$$\begin{aligned}&\frac{\Delta t^*}{\varepsilon^2 Re}<0.595 \quad \text{for an Euler explicit scheme}\\ &\frac{\Delta t^*}{\varepsilon^2 Re}<0.297 \quad \text{for a second-order Adams–Bashforth scheme}\end{aligned} \tag{50}$$

where Δt^* is the dimensionless time step. In this study, the spatial resolution for the computation of the free surface is set to be looser than the spatial resolution for the vorticity field. After a series of numerical experiments, we find that in the present model the stability is constrained by the vorticity computation and Equation (50) can be used as the stability criterion of the present model.

4. NUMERICAL EXAMPLES

This section summarizes a number of studies to verify the proposed model. In Section 4.1 the inviscid part of the numerical method is examined using a calculation of solitary wave propagation in a uniform channel. Its main purpose is to verify the ability of the method to simulate the motion of nonlinear waves. A further test reported in Section 4.2 is implemented by comparing the numerical results with theoretical solutions for a moving line vortex interacting with the free surface. In this test we may verify the ability of the method to simulate the free-surface deformation induced by the vortex in the fluid. In Section 4.3 a case of periodic water waves travelling over a rectangular submerged obstacle is performed, and comparisons are made with respect to experimental measurements provided by Ting and Kim [37]. In this test we may verify the comprehensive capacity of the present method. The convergence study of refinements in the spatial and temporal discretization is also presented in Section 4.3.

4.1. Solitary wave propagation in a uniform channel

The numerical test is implemented in a uniform channel whose length is $50h$. Sponge layers are placed at $0\leqslant x/h\leqslant 1$ and $49\leqslant x/h\leqslant 50$ with $v_d=10$. A solitary wave propagating from left to right

DOI: 10.1002/fld

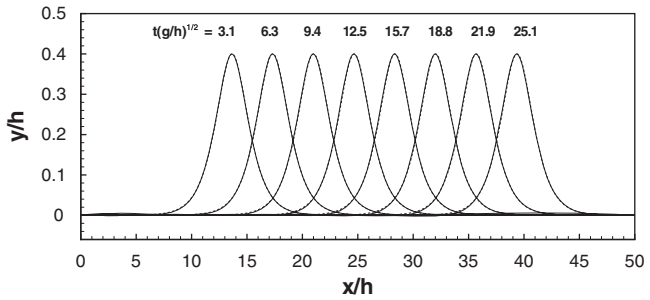

Figure 3. The numerical results of solitary wave propagating on constant depth, evaluated by the present scheme (——) and Tanaka's method (– – –).

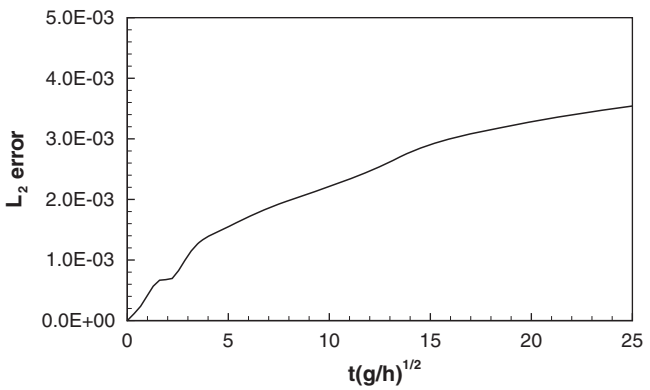

Figure 4. L_2-norm error of the computed free-surface elevation of solitary wave propagation.

with wave height $H/h=0.4$ is simulated. The panel length at the free surface is $\Delta x=0.0625h$ initially, and the time step is 0.01. The initial free-surface elevation and velocity potential are obtained by Tanaka's method [38], which can compute the exact solitary wave solution. The method of image is applied to enforce the no-penetration boundary condition on the bottom.

Figure 3 shows the comparison between the free-surface profiles evaluated by the present method and those by Tanaka's method. The L_2-norm error of the computed free-surface elevation in the time evolution, as compared with the exact solution, is presented in Figure 4. The L_2-norm error is defined as

$$L_2(y_F)=\sqrt{\frac{1}{N_F}\left[\frac{1}{H^2}\sum_{i=1}^{N_F}(y_F^{\text{exact}}-y_F^{\text{numerical}})^2\right]}$$

where N_F is the number of panels at the free surface. The two figures reveal that the computational results including both wave shape and wave phase agree with Takana's solution very well, and the sponge layers successfully absorb the small, out-going disturbances.

DOI: 10.1002/fld

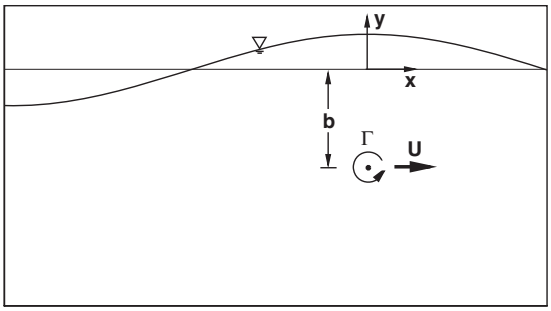

Figure 5. Schematic diagram of the surface wave generated by a moving line vortex.

4.2. Moving submerged line vortex

In a deep channel ($h \to \infty$) with inviscid fluid, a line vortex with constant strength Γ moves at constant velocity U in the direction perpendicular to the x-axis and at a fixed distance b below the undisturbed free surface, as shown in Figure 5. In order to perform an identical simulation with the linear theoretical solution proposed by Salvesen [39], the nonlinear terms in the evolution equations for z_F and γ_F are omitted. The field length is selected to be 22 with sponge layers at $-11 \leqslant x \leqslant -10$ and $10 \leqslant x \leqslant 11$, and the water depth is infinite. Time step is set to be 0.01, and at the free surface the initial panel length $\Delta x = 0.2$. Positive and negative circulations, $\Gamma = \pm\pi$, are considered, and the velocity of the line vortex is 3. The initial position of the line vortex is $(-9.0, -1.5)$.

Figures 6(a) and (b) demonstrate the comparisons between the wave profiles evaluated by the numerical model and those by the analytic solution. Figure 7 shows the L_2-norm error of the computed free-surface elevation, as compared with the exact solution. It can be observed that the numerical results and analytic solutions are in good agreement.

4.3. Periodic waves passing over a rectangular submerged obstacle

4.3.1. Description of computational setup. The experiment presented in [37] was conducted in a 37-m long, 0.91-m wide and 1.22-m deep wave tank with a permeable wave absorbing beach downstream. A rectangular obstacle of height $d = 30.48$ cm and width $l = 60.96$ cm was placed on the bottom of the tank. Its center was situated at $x = 0$ m and the wave generator was located at $x = -10.7$ m. The water depth h is 60.96 cm, the incident wave height H is 5.85 cm and the incident wave period T is 4.0 s.

In the numerical computation the characteristic velocity scale evaluated from the incoming wave condition [40] is 0.49 m/s, the characteristic length scale is 0.6096 m and the Reynolds number $Re = 3.0 \times 10^5$. The computational domain is confined within $x/h = -23.0$–11.5. Sponge layers are placed at $-23.0 \leqslant x/h \leqslant -19.7$ and $8.2 \leqslant x/h \leqslant 11.5$ with $v_d = 40$. The fluid is initially at rest, and wave train is generated using the internal wave-maker with the source function for the second-order Stokes wave.

4.3.2. Particle remeshing with mapping of the physical domain. From the experimental result one may observe that vorticity is located in the vicinity of the upper corners of the obstacle. Thus, it would be more efficient to set high resolution near the upper corners of the obstacle and coarser

DOI: 10.1002/fld

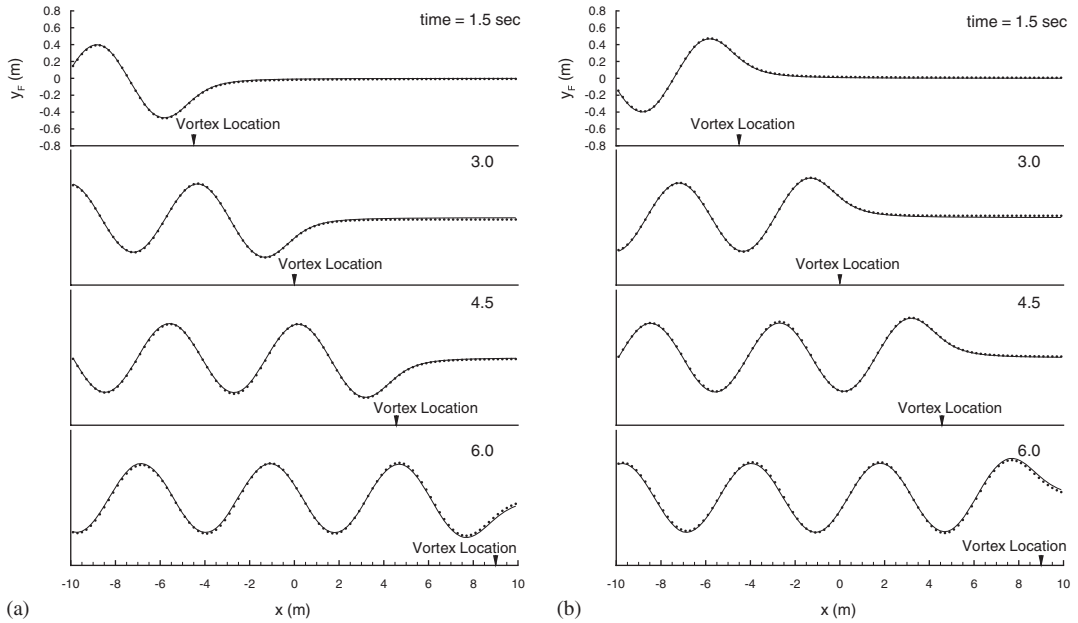

Figure 6. Wave profile generated by the moving line vortex at various times evaluated by the numerical model (——) and the analytic solution (●●●): (a) $\Gamma=-\pi$ and (b) $\Gamma=\pi$.

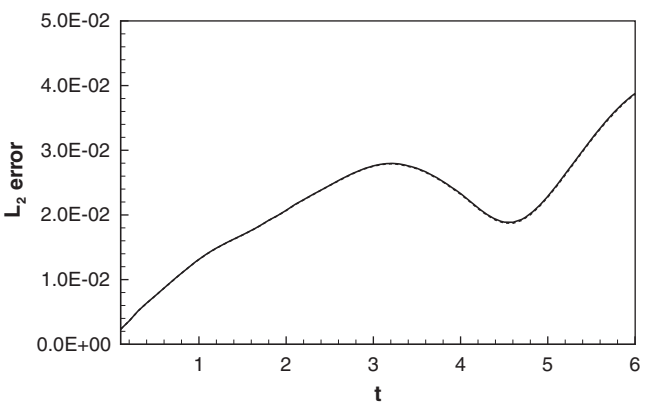

Figure 7. L_2-norm error of the computed free-surface elevation of the moving line vortex: $\Gamma=\pi$ (——), $\Gamma=-\pi$ (– – –).

resolution in the far region. To achieve this, using an appropriate mapping the physical domain with spatially varying resolution can be mapped onto a regular indicial lattice [26, 41]. We denote by $\mathbf{x}$ locations in the physical space with variable blob size, and by $\boldsymbol{\xi}=(\xi,\eta)$ locations in the mapped coordinates, where the grid size is uniform. In this case the following mapping is applied:

$$\xi(z)+\mathrm{i}\,\eta(z)=K_0(z-z_0)^{2/3} \tag{51}$$

DOI: 10.1002/fld

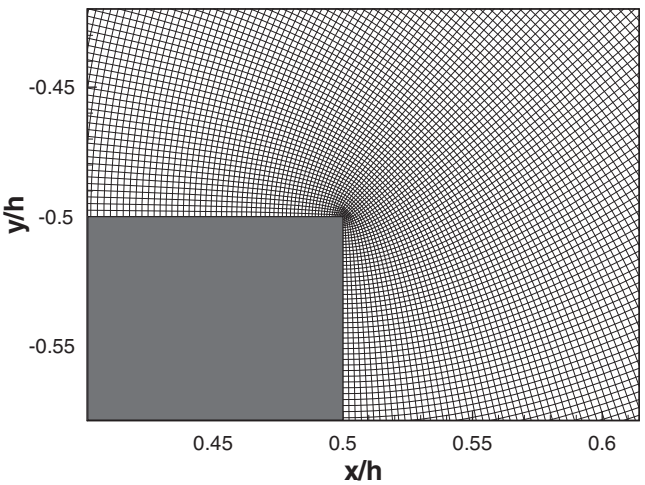

Figure 8. Redistribution mapping for the periodic waves travelling over a rectangular obstacle.

Table I. Parameters of the cases for convergence study.

	Δt^*	N_B	N_F
Case 1	0.025	750	600
Case 2	0.01	920	780
Case 3	0.005	1160	960

where $z = x + iy$, z_0 is the position of the upper corner, which is closer to z than another. The constant K_0 is chosen so that the length of the smallest cell is approximately equal to $\sqrt{2\Delta t^*/Re}$. After each redistribution, new particles have position $(i+\frac{1}{2}, j+\frac{1}{2})$ in the mapped domain. The area associated with the particle in the physical space is

$$S_p = J(\xi)$$

where J denotes the Jacobian determinant of the mapping. Here an overlapping ratio $\varepsilon/h_p = 1$ is used and thus $\varepsilon = \sqrt{S_p}$. The mesh of the redistribution mapping is illustrated in Figure 8.

One should note that this is a local mapping for the region near a single upper corner of the rectangular obstacle; therefore, it is necessary to link two local mappings (for two upper corners) by their superposition.

4.3.3. Convergence study. The convergence of the numerical solution was examined by varying the parameters of the numerical model, such as the core size ε, the time step Δt^*, the number of panels on the solid wall N_B and on the free surface N_F. Because the smallest panel length on the solid surface is equal to $\sqrt{2\Delta t^*/Re}$ and an overlap ratio $\varepsilon/h_p = 1$ was used, the first three parameters listed above were linked. Three cases with different Δt^* and N_F were computed (see Table I), and the results of free-surface elevation, vorticity field and streamlines were used to

DOI: 10.1002/fld

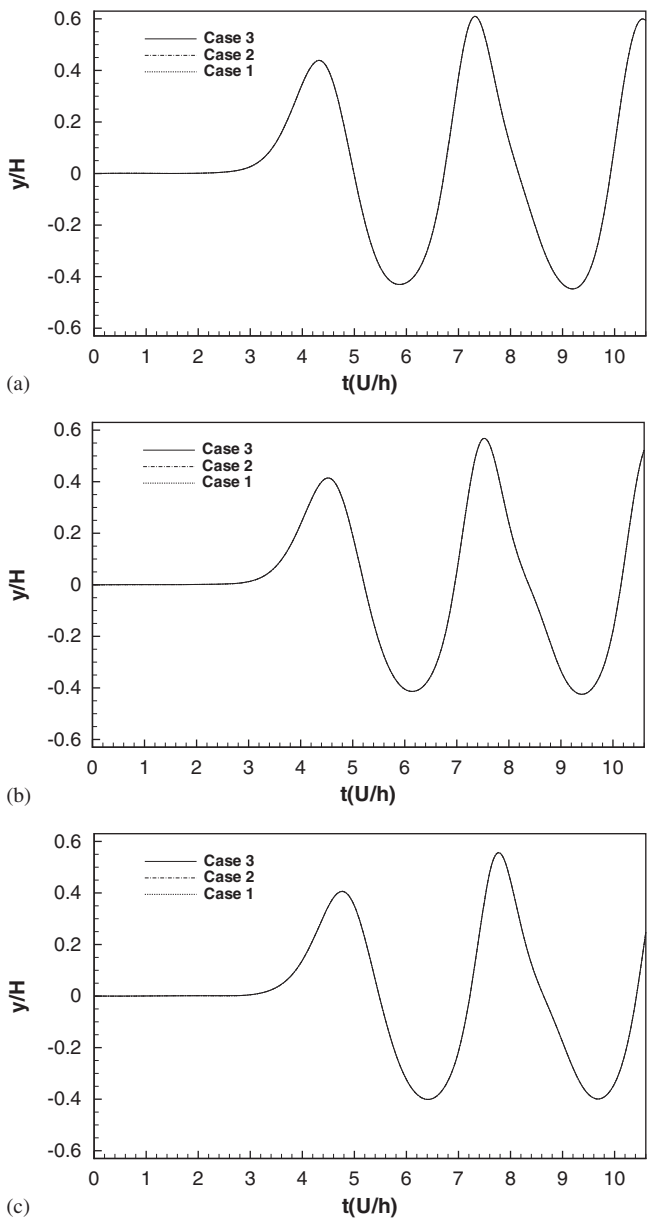

Figure 9. Effect of variable resolution on the free-surface elevation.

monitor the convergence. In these cases, particle remeshing is performed every two time steps, and the sub-grid modelling for eddy viscosity with $C_s = 0.15$ is applied.

In Figure 9 we present the time histories of the free-surface elevation at various measuring points: (a) $x/h = -1$, (b) $x/h = 0$ and (c) $x/h = 1$. The result reveals that the computation of the free-surface elevation is relatively insensitive to these parameters. In Figure 10(a) the

DOI: 10.1002/fld

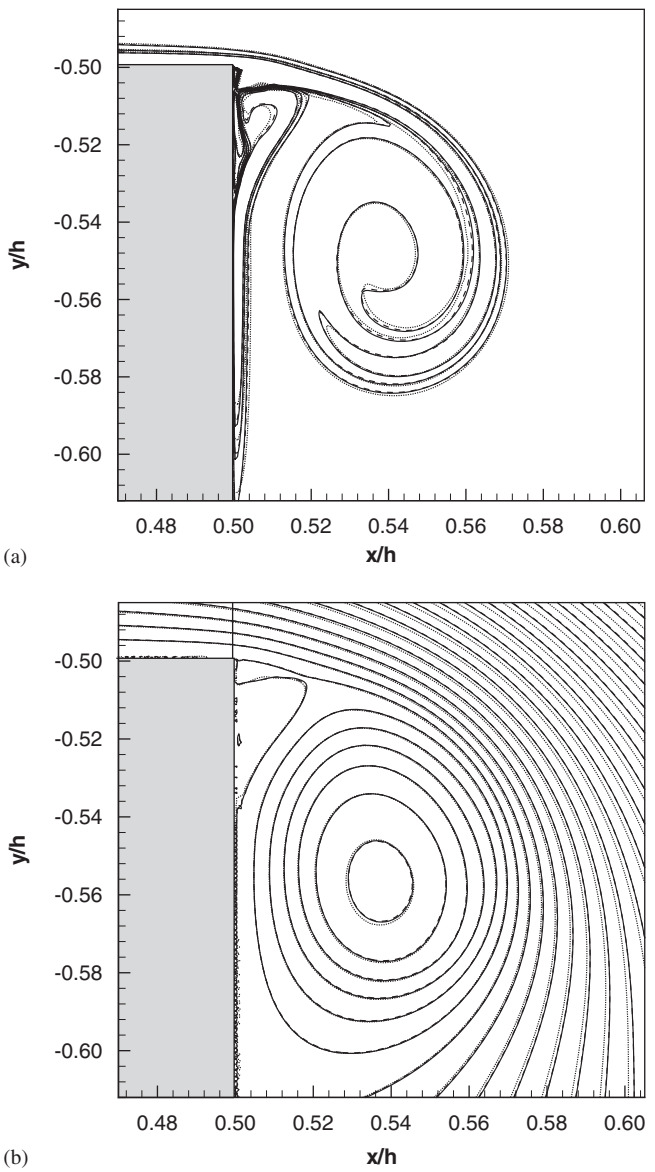

Figure 10. Effect of variable resolution on (a) the vorticity contours and (b) the streamlines: (···) Case 1; (– – –) Case 2; and (——) Case 3.

dimensionless vorticity contours of $(0, \pm 10, \pm 30, \ldots)$ and (b) the dimensionless streamlines of $(0, \pm 0.002, \pm 0.004, \ldots)$ at $t(U/h) = 4.9$ are presented. It shows that the results of Cases 2 and 3 are in good agreement.

In order to demonstrate the validity of the method with variable blob size using the proposed mapping, the result obtained from the computation using non-variable blobs is also presented. Its computational parameters are $\Delta t^* = 0.005$, $N_B = 3000$ and $N_F = 960$, and the remeshing

DOI: 10.1002/fld

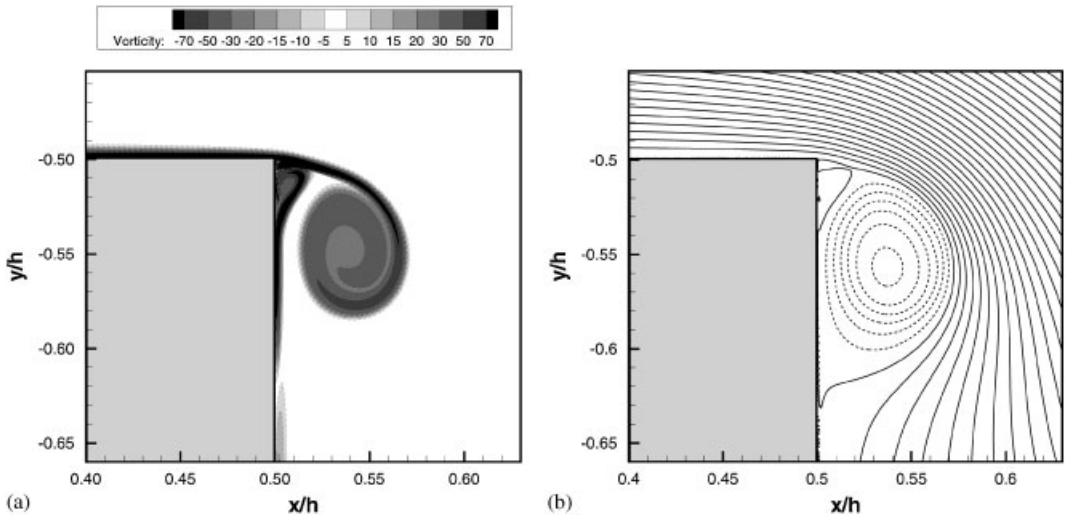

Figure 11. Computational result of (a) vorticity and (b) streamline contours by variable blob size for periodic waves travelling over a submerged obstacle.

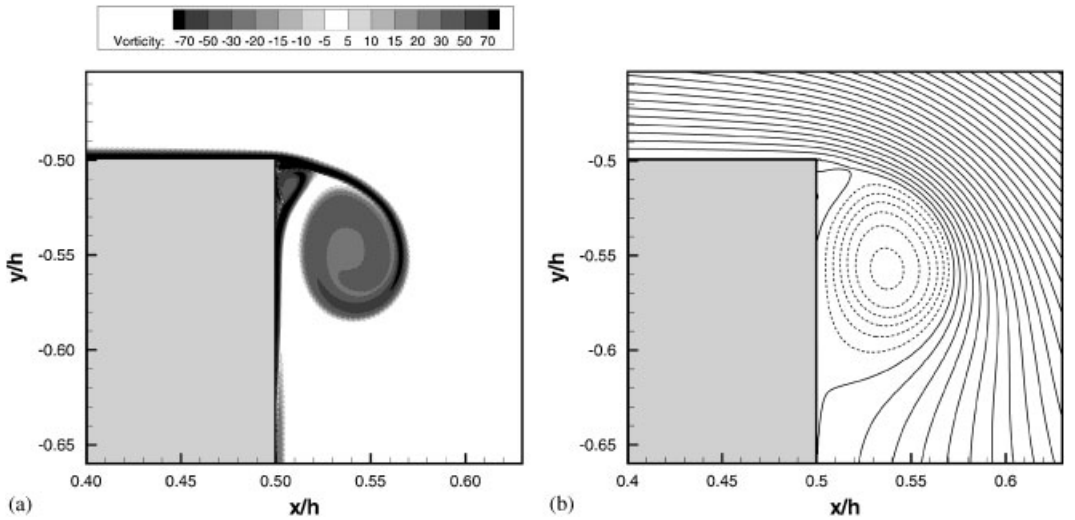

Figure 12. Computational result of (a) vorticity and (b) streamline contours by uniform blob size for periodic waves travelling over a submerged obstacle.

frequency is two time steps. Figures 11 and 12 show the vorticity contours and streamlines at $t(U/h)=4.9$ computed by variable blobs (Case 3) and by uniform blobs, respectively. It can be observed that two results are in good agreement. The particle locations in both cases are presented in Figure 13, and the saving on computational elements up to time $t(U/h)=4.9$ is shown in Figure 14.

DOI: 10.1002/fld

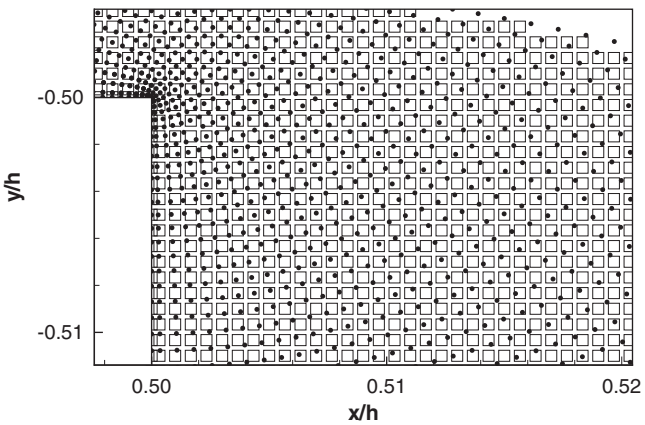

Figure 13. Particle locations for periodic waves travelling over a submerged obstacle: variable size blobs (•) and constant size blobs (□).

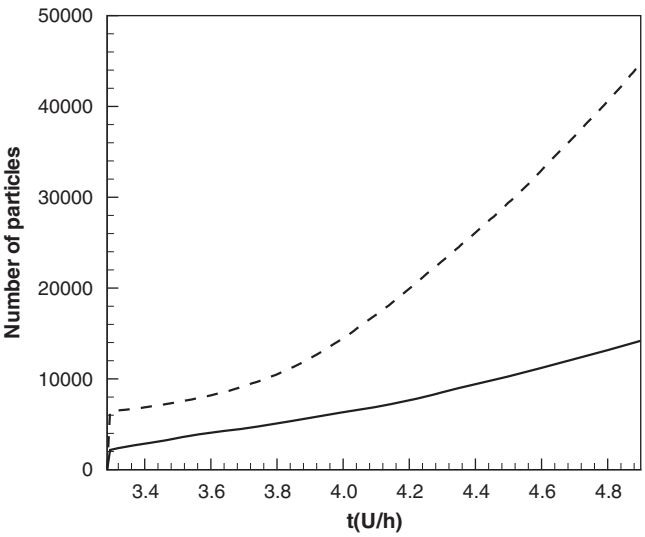

Figure 14. Number of particles as a function of time for periodic waves travelling over a submerged obstacle: variable size blobs (——) and constant size blobs (– – –).

4.3.4. Results and verifications. During a wave period the number of particles goes from ∼15 000 to ∼25 000, and the total run time is approximately 6 h on a personal computer with a single 2.66 GHz CPU. The computational free-surface elevations at different phases in a wave period are shown in Figure 15, in which t_0 is the time when the wave crest arrives at the left wall of the obstacle. We compare the computed amplitudes of the first three harmonics with the experimental data in Figure 16. Good agreement is observed from this comparison.

DOI: 10.1002/fld

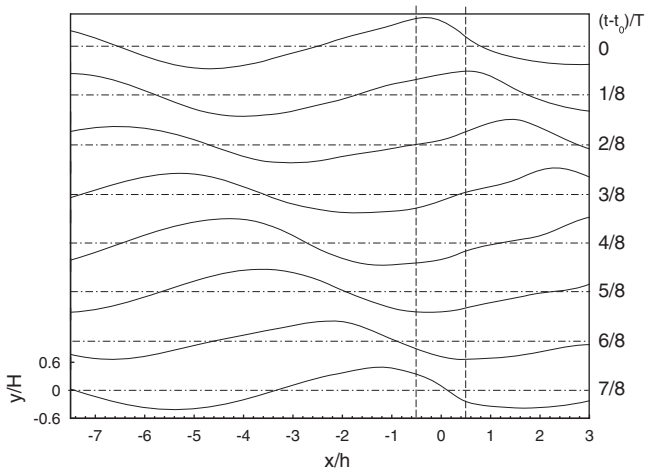

Figure 15. Free-surface elevations at different phases for periodic waves passing over a submerged rectangular obstacle.

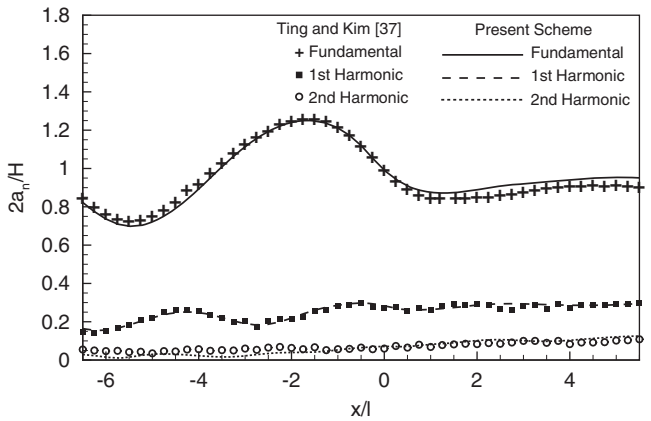

Figure 16. Variations of fundamental and harmonic wave amplitudes for periodic waves passing a submerged rectangular obstacle.

The vorticity fields at different phases are presented in Figure 17. It shows that when the flow direction changed, former recirculating zone dissipates due to the convection of the reversed flow and the diffusion of vorticity. The growth and dissipation of recirculating zones are periodic, and the vortices are trapped in confined regions near the two upper corners of the obstacle. Figure 18 shows the comparisons of the velocity field at different phases between the numerical results and the laboratory measurements and indicates that the present method captures the flow patterns reasonably well. In order to compare the present results with those by a grid-based scheme, in Figure 19 we show the velocity fields presented by Hsu *et al*. [18], who simulated the same experiment using a finite-analytic method to solve the RANS equations with the k–ε turbulence

DOI: 10.1002/fld

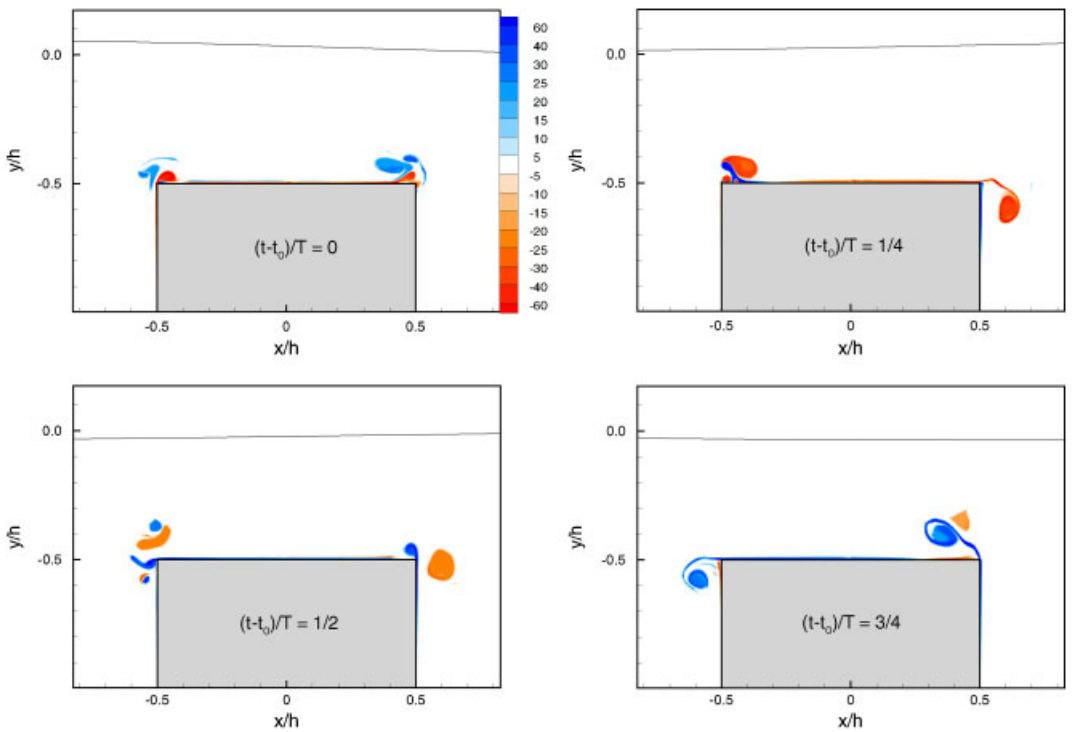

Figure 17. Vorticity contours and free-surface profiles at different phases for periodic waves passing a submerged rectangular obstacle.

closure. It can be observed that the present method provides more reasonable results. This may be attributed to the relatively higher resolution of our computation.

To test whether the sub-grid eddy viscosity is necessary, the vorticity contours as computed without the sub-grid modelling are shown in Figure 20. One may observe that lack of the sub-grid eddy viscosity causes significant oscillation of vorticity. In fact, from the results of numerical tests with different incoming wave conditions we may find that without the use of eddy viscosity a non-periodic flow pattern appears because the vorticity dissipation is underestimated. This appears to violate the observation in laboratory experiments.

5. CONCLUSIONS

The aim of this study was to establish a 2-D numerical model that combines the vortex method and the boundary integral method to simulate the interaction of surface water waves with a submerged obstacle. Generation of vorticity on the free surface is neglected.

The inviscid part of the numerical method is tested using a calculation of solitary wave propagation in a uniform channel. Surface elevation is compared with results of an exact solution evaluated numerically, finding good agreement. A further test is performed by comparing numerical results with theoretical solutions for a moving line vortex interacting with the free surface. Good agreement

DOI: 10.1002/fld

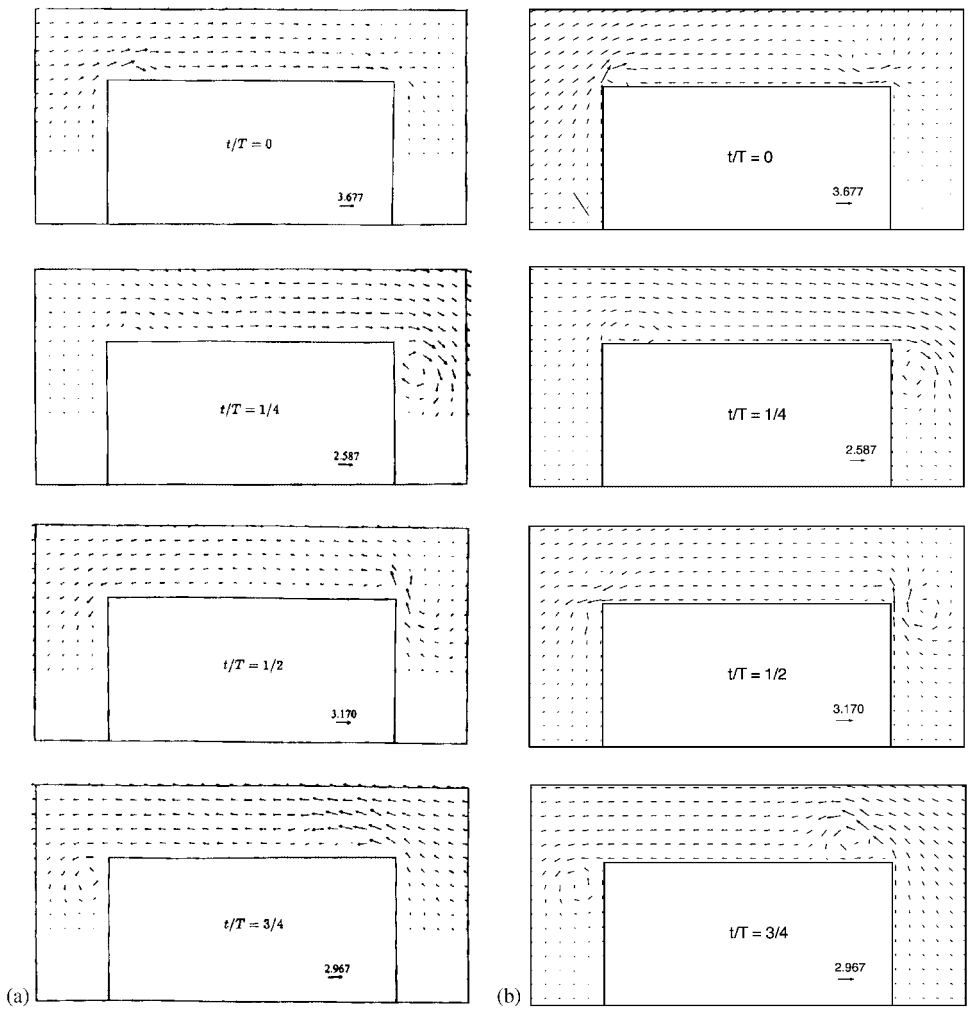

Figure 18. Comparisons of the velocity fields at different phases between numerical results and laboratory measurements: (a) experiments by Ting and Kim [37] and (b) present model.

in the wave profiles is obtained. The full numerical method is used to compute the flow resulting from periodic water waves travelling over a submerged rectangular obstacle, and comparisons are made with respect to experimental results. The overall agreement is reasonably well.

The major advantage of the proposed numerical method is the ability of a boundary integral method to solve the free-surface motion and the essentially grid-free nature of the Lagrangian vortex method for the vorticity field. A boundary integral method is a predominant scheme for simulating a moving boundary problem because only grid points on the boundaries of the fluid domain are needed. On the other hand, inside the fluid domain, describing the flow in terms of vorticity-carrying elements is desirable due to the fact that the rotational flow field is usually

DOI: 10.1002/fld

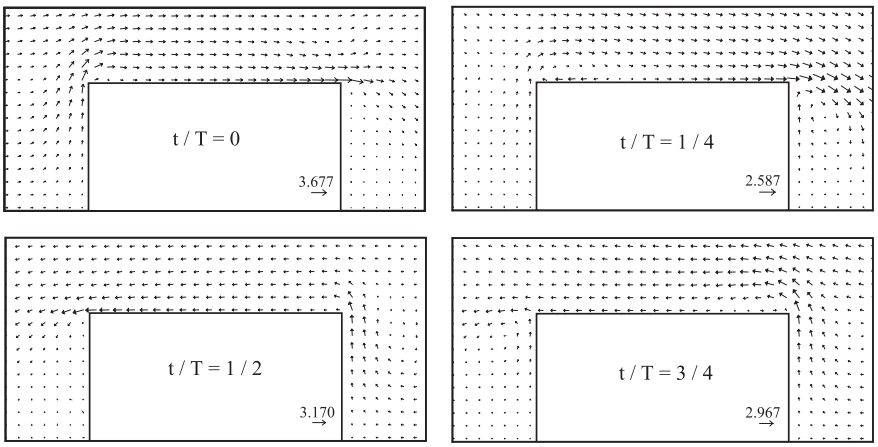

Figure 19. Computational results of Hsu *et al.* [18] for periodic waves passing over a submerged rectangular obstacle.

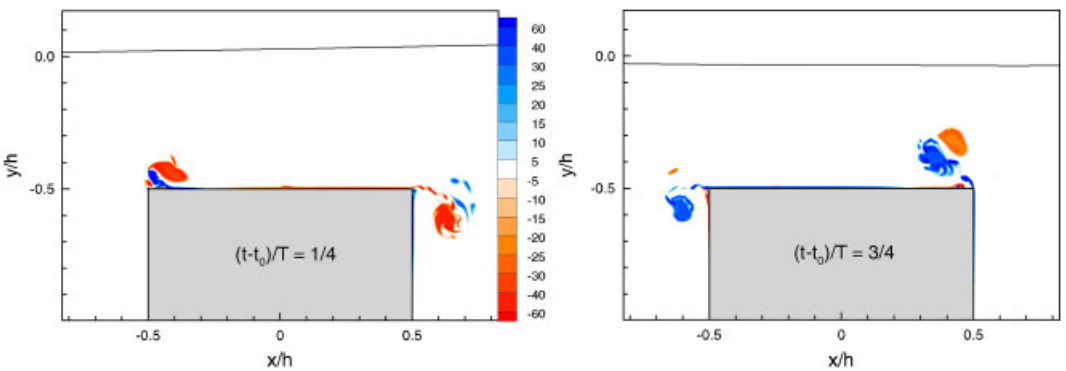

Figure 20. Vorticity contours for periodic waves passing a submerged rectangular obstacle, as computed without sub-grid modelling.

confined inside small regions around submerged bodies; therefore, predominantly compact computational domains can be used, in comparison with primitive variable formulations.

APPENDIX A: HELMHOLTZ DECOMPOSITION AND THE CORRESPONDING INTEGRAL FORMULATIONS

The Helmholtz decomposition theorem states that an arbitrary differentiable velocity field **u** can be decomposed into its irrotational and rotational part as (for 2-D flow):

$$\mathbf{u} = \nabla\phi + \nabla \times (\psi\hat{\mathbf{k}}) \tag{A1}$$

DOI: 10.1002/fld

where ϕ and $\psi\hat{\mathbf{k}}$ are scalar and vector potentials, respectively. The integral formulation of the decomposition for incompressible fluid flow may be expressed as [42]

$$\mathbf{u}(\mathbf{x}) = \int_V \omega(\mathbf{x}')\hat{\mathbf{k}} \times \nabla G \, \mathrm{d}\mathbf{x}' + \nabla \int_S G \, \hat{\mathbf{n}}(\mathbf{x}') \cdot \Delta\mathbf{u}(\mathbf{x}') \, \mathrm{d}\mathbf{x}' - \nabla \times \int_S G \, \hat{\mathbf{n}}(\mathbf{x}') \times \Delta\mathbf{u}(\mathbf{x}') \, \mathrm{d}\mathbf{x}' \tag{A2}$$

where S is the boundary of V, $\Delta\mathbf{u} = \mathbf{u}_2 - \mathbf{u}_1$ (where the subscripts 1 and 2 indicate the two sides of S, which are in the interior and exterior of the fluid flow domain, respectively) and the unit normal vector $\hat{\mathbf{n}}$ points from side 1 to side 2. One may find that the boundary integrals over S give the potential velocity induced by sources and vortex sheets represented by the inner product $\hat{\mathbf{n}} \cdot \Delta\mathbf{u}$ and the cross product $\hat{\mathbf{n}} \times \Delta\mathbf{u}$, respectively. Because on a solid wall the no-slip condition ($\Delta\mathbf{u} = 0$) applies, the distributions of source or vortex sheet are absent. At the free surface the discontinuity of density induces a jump in tangential velocity across the interface with continuous normal velocity; hence, a vortex sheet exists along the free surface. Since in 2-D flow the vortex-sheet strength is related to the arc-length derivatives of the dipole strength [24], Equation (A2) can be rewritten as

$$\begin{aligned} \mathbf{u}(\mathbf{x}) &= \int_V \omega(\mathbf{x}')\hat{\mathbf{k}} \times \nabla G \, \mathrm{d}\mathbf{x}' + \int_{S_\mathrm{F}} \mu(\mathbf{x}') \frac{\partial G}{\partial n(\mathbf{x}')} \, \mathrm{d}\mathbf{x}' \\ &= \int_V \omega(\mathbf{x}')\hat{\mathbf{k}} \times \nabla G \, \mathrm{d}\mathbf{x}' + \int_{S_\mathrm{F}} \gamma_\mathrm{F}(\mathbf{x}')\hat{\mathbf{k}} \times \nabla G \, \mathrm{d}\mathbf{x}' \end{aligned} \tag{A3}$$

ACKNOWLEDGEMENTS

This study is supported by the National Science Council of R.O.C. under Contracts NSC 92-2611-E-002-030 and NSC 93-2611-E-002-012.

REFERENCES

1. Lamb H. *Hydrodynamics.* Cambridge University Press: Cambridge, U.K., 1932.
2. Newman JN. Reflection and transmission of water waves past long obstacles. *Journal of Fluid Mechanics* 1965; **23**:399–415.
3. Mei CC, Black JL. Scattering of surface waves by rectangular obstacles in waters of finite depth. *Journal of Fluid Mechanics* 1969; **38**:499–511.
4. Massel SR. Harmonic generation by waves propagating over a submerged step. *Coastal Engineering* 1983; **7**:357–380.
5. Baker GR, Meiron DI, Orszag SA. Generalized vortex methods for free surface flow problems II: radiating waves. *Journal of Scientific Computing* 1989; **4**(3):237–259.
6. Grue J. Nonlinear water wave at a submerged obstacle. *Journal of Fluid Mechanics* 1992; **244**:455–476.
7. Rey V, Belzons M, Guazzelli E. Propagation of surface gravity waves over a rectangular submerged bar. *Journal of Fluid Mechanics* 1992; **235**:453–479.
8. Yenug RW, Vaidhyanathan M. Non-linear interaction of water waves with submerged obstacles. *International Journal for Numerical Methods in Fluids* 1992; **14**:1111–1130.
9. Grilli ST, Losada MA, Martin F. Characteristics of solitary wave breaking induced by breakwaters. *Journal of Waterway, Port, Coastal and Ocean Engineering* 1994; **120**:609–628.
10. Guyenne P, Nicholls DP. Numerical simulation of solitary waves on plane slopes. *Mathematics and Computers in Simulation* 2005; **69**:269–281.
11. Chan IC, Huang LH, Hsieh PC. Analysis of water waves passing over a submerged rectangular dike. *Journal of Engineering Mechanics* (ASCE) 2003; **129**(6):613–626.

DOI: 10.1002/fld

12. Zhang DH, Chwang AT. Numerical study of nonlinear shallow water waves produced by a submerged moving disturbance in viscous flow. *Physics of Fluids* 1996; **8**(1):147–155.
13. Zhang DH, Chwang AT. On solitary waves forced by underwater moving objects. *Journal of Fluid Mechanics* 1999; **389**:119–135.
14. Tang CJ, Chang JH. Application of local grid refinement to vortex motion due to a solitary wave passing over a submerged body. *International Journal for Numerical Methods in Fluids* 2002; **38**:609–624.
15. Sue YC, Chern MJ, Hwang RR. Interaction of nonlinear progressive viscous waves with a submerged obstacle. *Ocean Engineering* 2005; **32**:893–923.
16. Helenbrook BT, Martinelli L, Law CK. A numerical method for solving incompressible flow problems with a surface of discontinuity. *Journal of Computational Physics* 1999; **148**:366–396.
17. Zwart PJ, Raithby GD, Raw MJ. The integrated space-time finite volume method and its application to moving boundary problems. *Journal of Computational Physics* 1999; **154**:497–519.
18. Hsu TW, Hsieh CM, Hwang RR. Using RANS to simulate vortex generation and dissipation around impermeable submerged double breakwaters. *Coastal Engineering* 2004; **51**:557–579.
19. Masud A, Hughes TJR. A space-time Galerkin/least-squares finite element formulation of the Navier–Stokes equations for moving domain problems. *Computer Methods in Applied Mechanics and Engineering* 1997; **146**:91–126.
20. Idelsohn SR, Onate E, Sacco C. Finite element solution of free-surface ship-wave problems. *International Journal for Numerical Methods in Engineering* 1999; **45**:503–528.
21. Lo DC, Young DL. Arbitrary Lagrangian–Eulerian finite element analysis of free surface flow using a velocity–vorticity formulation. *Journal of Computational Physics* 2004; **195**:175–201.
22. Cottet GH, Koumoutsakos P. *Vortex Methods*: *Theory and Applications*. Cambridge University Press: Cambridge, U.K., 2000.
23. Lundgren T, Koumoutsakos P. On the generation of vorticity at a free surface. *Journal of Fluid Mechanics* 1999; **382**:351–366.
24. Baker GR, Meiron DI, Orszag SA. Generalized vortex methods for free-surface flow problems. *Journal of Fluid Mechanics* 1982; **123**:477–501.
25. Telste JG. Potential flow about two counter-rotating vortices approaching a free surface. *Journal of Fluid Mechanics* 1989; **201**:259–278.
26. Ploumhans P, Winckelmans GS. Vortex methods for high-resolution simulations of viscous flow past bluff bodies of general geometry. *Journal of Computational Physics* 2000; **165**:354–406.
27. Greengard L, Rohklin V. A fast algorithm for particle simulations. *Journal of Computational Physics* 1987; **73**:325.
28. Ambrosiano J, Greengard L, Rohklin V. The fast multipole method for gridless particle simulation. *Computer Physics Communications* 1988; **48**:117–125.
29. Pfalzner S, Gibbon P. *Many-Body Tree Methods in Physics.* Cambridge University Press: New York, U.S.A., 1996.
30. Monaghan JJ. Extrapolating B-splines for interpolation. *Journal of Computational Physics* 1985; **60**:253–262.
31. Longuet-Higgins MS, Cokelet ED. The deformation of steep surface waves on water. I. A numerical method of computation. *Proceedings of the Royal Society of London*, *Series A* 1976; **350**:1–26.
32. Lin P, Liu PLF. Internal wave-maker for Navier–Stokes equations models. *Journal of Waterway*, *Port*, *Coastal and Ocean Engineering* 1999; **125**(4):207–215.
33. Dean RG, Dalrymple RA. *Water Wave Mechanics for Engineers and Scientists.* World Scientific: Singapore, 1991.
34. Smagorinsky J. General circulation experiments with the primitive equations, part I: the basic experiment. *Monthly Weather Review* 1963; **91**:99–164.
35. Mansfield JR, Knio OM, Meneveau C. A dynamic LES scheme for the vorticity transport equation: formulation and *a priori* tests. *Journal of Computational Physics* 1998; **145**:693–730.
36. Ploumhans P. Simulation of high-Reynolds number flows past bluff bodies using vortex and boundary element methods. *Ph.D. Thesis*, Université Catholique de Louvain, Belgium, 2001.
37. Ting FCK, Kim YK. Vortex generation in water waves propagating over a submerged obstacle. *Coastal Engineering* 1994; **24**:23–49.
38. Tanaka M. The stability of solitary waves. *Physics of Fluids* 1986; **29**:650.
39. Salvesen N. On higher-order wave theory for submerged two-dimensional bodies. *Journal of Fluid Mechanics* 1969; **38**:415–432.

DOI: 10.1002/fld

40. Chang KA, Hsu TJ, Liu PLF. Vortex generation and evolution in water waves propagating over a submerged rectangular obstacle. Part II: cnoidal waves. *Coastal Engineering* 2005; **52**:257–283.
41. Cottet GH, Koumoutsakos P, Ould Salihi ML. Vortex methods with spatially varying cores. *Journal of Computational Physics* 2000; **162**:164–185.
42. Morino L. Helmholtz and Poincaré potential-vorticity decompositions for the analysis of unsteady compressible viscous flows. In *Boundary Element Methods in Nonlinear Fluid Dynamics*, Banerjee PK, Morino L (eds). Elsevier: New York, U.S.A., 1990; 1–54.

DOI: 10.1002/fld